



HAL
open science

EBSD analysis of MgB₂ bulk superconductors

Anjela Koblischka-Veneva, Michael Rudolf Koblischka, Jörg Schmauch, Kazuo Inoue, Muralidhar Miryala, Kévin Berger, Jacques Noudem

► **To cite this version:**

Anjela Koblischka-Veneva, Michael Rudolf Koblischka, Jörg Schmauch, Kazuo Inoue, Muralidhar Miryala, et al.. EBSD analysis of MgB₂ bulk superconductors. *Superconductor Science and Technology*, 2016, 29 (4), 044007, 10 p. 10.1088/0953-2048/29/4/044007 . hal-01270308

HAL Id: hal-01270308

<https://hal.science/hal-01270308v1>

Submitted on 6 Feb 2016

HAL is a multi-disciplinary open access archive for the deposit and dissemination of scientific research documents, whether they are published or not. The documents may come from teaching and research institutions in France or abroad, or from public or private research centers.

L'archive ouverte pluridisciplinaire **HAL**, est destinée au dépôt et à la diffusion de documents scientifiques de niveau recherche, publiés ou non, émanant des établissements d'enseignement et de recherche français ou étrangers, des laboratoires publics ou privés.

EBSA analysis of MgB₂ bulk superconductors

A. Koblichka-Veneva¹, M.R. Koblichka^{1*}, J. Schmauch¹, K. Inoue², M. Muralidhar²,
K. Berger³, J. Noudem⁴

¹ – *Experimental Physics, Saarland University, P.O.Box 151150, 66041 Saarbrücken, Germany*

² – *Superconducting Materials Laboratory, Department of Materials Science and Engineering, Shibaura Institute of Technology 3-7-5 Toyosu, Koto-ku, Tokyo 135-8548, Japan*

³ – *GREEN, University of Lorraine, Nancy, France*

⁴ – *CRISMAT-CNRS, Cherbourg, France*

Abstract. The grain orientation, the texture and the grain boundary misorientations are important parameters for the understanding of the magnetic properties of the bulk MgB₂ samples intended for super-magnet applications. Such data can be provided by electron backscatter diffraction (EBSA) analysis. However, as the grain size of the MgB₂ bulks is preferably in the 100-200 nm range, the common EBSA technique working in reflection operates only properly on highly dense samples. In order to achieve a reasonably good Kikuchi pattern quality on all samples, we apply here the newly developed transmission EBSA (t-EBSA) technique to several bulk MgB₂ samples. This method requires the preparation of TEM slices by means of focused ion-beam milling, which are then analyzed within the SEM, operating with a specific sample holder. We present several EBSA mappings of samples prepared with different techniques and at various reaction temperatures.

Keywords: MgB₂, microstructure, EBSA

PACS: 68.37.Hk, 74.70.Ad, 74.25.Sv

*Corresponding author: M.R. Koblichka

e-mail: m.koblichka@mx.uni-saarland.de

Phone: +49 681 302 4555, Fax: +49 681 302 3790

1. Introduction

Applications of bulk superconductors like magnetic bearings, couplings and trapped field magnets ("super-magnets") require the fabrication of large sample sizes, as the maximum achievable trapped field depends on the sample size [1]. For this purpose, the superconducting material involved should be cheap, and to be produced in a simple, cost-effective manner. MgB_2 fulfills this demand being free of rare-earth materials which are expensive, and large samples can be produced by a conventional sintering technique. Therefore, MgB_2 is a good candidate for a large variety of applications [2-6]. Strong currents can flow in polycrystalline MgB_2 samples due to strongly-linked grains, and the grain boundaries are strong flux pinning sites as in conventional Nb_3Sn material [7]. Of course, the parameters of the sintering process must be properly optimized in order to produce a material with high critical current density [8-10]. Therefore, a thorough microstructure characterization of MgB_2 samples prepared using different techniques and at different reaction temperatures is necessary to understand the resulting superconducting properties. An important tool to achieve this goal is provided by the electron backscatter diffraction (EBSD) technique. However, up to now there are only some reports using this technique in the literature on MgB_2 material [11-13], which is strongly linked to the problems arising in the sample preparation stage. Here, we present a solution to these problems by means of the newly developed transmission EBSD technique (t-EBSD) [14,15], which is based on the fabrication of TEM slices by means of focused ion-beam milling. The TEM slices are then investigated in the SEM using a special sample holder. This approach was recently carried out in the literature on nano-grained MgB_2 [16] and graphene-oxide doped MgB_2 samples [17].

This paper is organized as follows: In Sec. 2, the sample and sample surface preparation and the preparation of the TEM slices required for EBSD are outlined. In Sec. 3, we describe firstly the motivation for the microstructure analysis. Then, the EBSD results are presented and discussed. Finally, some conclusions are drawn.

2. Experimental procedure

2.1 Sample and surface preparation

The polycrystalline MgB₂ samples from SIT, Tokyo were fabricated by using a low-cost, in-situ solid state reaction. Mg and B powders of high purity were pressed into pellets and sintered under argon atmosphere at temperatures varying from 775 to 950 °C. All samples were kept at the target temperature for 3 h. More details on the preparation route and the respective x-ray data are given elsewhere [9,18].

The MgB₂ samples with high density (HD) were synthesized in a spark plasma sintering system in DC mode at a temperature of 1200 °C. The pulsed electric current (2000 A, 4 V) was passed through the sample under dynamic vacuum (10⁻³ bar) while a 50 MPa uniaxial pressure was applied. This preparation procedure is described in detail in Ref. [19].

The properties of all the samples investigated here are summarized in Table 1, presenting the sample names, the reaction type, the reaction temperature, the onset temperature of the superconducting transition, T_c , the measured current density at 20 K in self-field (measured by SQUID magnetometry), the normal-state resistivity [$\rho(41\text{ K})$], $\Delta\rho = \rho(300\text{ K}) - \rho(41\text{ K})$ as a measure for the grain connectivity, the EBSD type applied, the mean grain size and the grain boundary length (as determined by EBSD). The T_c data stem from resistance measurements on the samples; for more details see Ref. [20]. The EBSD measurements are discussed in Sec. 3 below.

For the magnetic measurements, small specimens with dimensions of $1.5 \times 1.5 \times 0.5\text{ mm}^3$ were cut from the bulk MgB₂ samples using a diamond saw. The magnetic data were recorded using a MPMS 7XL SQUID magnetometer from Quantum Design.

For the microstructure analysis, the sample surfaces were polished mechanically with SiO₂ papers, diamond paste and Struers SiO₂ OPS suspension to a total roughness of several nanometers. Details of the polishing procedure are described in Ref. [21]. For the EBSD analysis, the mechanically polished surfaces of the samples were further treated by low-angle argon ion-polishing (5 KeV, 5 min) to further

improve the image quality of the Kikuchi patterns as described in Ref. [22] for the investigation of ferrite samples.

The TEM slices for the t-EBSD measurements were produced by focused-ion beam (FIB) milling in a dual-beam FIB workstation (FEI) using a routine allowing for reduced surface damage. After lifting-off the TEM slice from the sample with the micromanipulator, the surface is ion-polished in a separate step by 2 KeV Ga-ions to a thickness of about 80 nm. This step serves to further reduce the preparation damage of the surface area and for a further thinning of the sample to be transparent to the electron beam. Figure 1 presents a typical TEM slice fabricated from a MgB₂ sample in two magnifications (inset).

2.2 EBSD

The EBSD analysis was performed in a JEOL 7000F SEM microscope equipped with a TSL (TexSEM Labs, UT) analysis unit. The Kikuchi patterns were generated at an acceleration voltage of 15 kV, and were recorded by means of a DigiView camera system. To produce a crystallographic orientation map, the electron beam was scanned over a selected surface area and the resulting Kikuchi patterns were indexed and analyzed automatically. This represents the common EBSD method working in reflection mode (hereafter called standard configuration). A detailed description of the measurement procedure can be found in Refs. [21,23]. Automated EBSD scans were performed with a step size down to 50 nm. The working distance in the standard configuration was set to 15 mm, while for t-EBSD a working distance of 5 mm was chosen.

Although any preparation technique for TEM samples can be used also for t-EBSD, the fabrication of TEM slices by FIB are best suited to select the proper sample area for the analysis. For t-EBSD, the TEM-slices were mounted in the SEM on a specially fabricated sample holder allowing for the correct 70° inclination of the sample required for EBSD. The stage with the sample holder is inclined to an angle of -20°, which enables together with the sample mounting the same detector position to be used for the EBSD detector as in the standard configuration. Here, the electron beam is passing through the

sample (transmission mode) and the electron cone is formed on the backside of the sample. The electron beam operates at 30 kV, and the working distance is set to 5 mm. The EBSD stepsize was 5 nm. An image of our sample holder and the entire arrangement within the SEM chamber is presented in Fig. 2.

2.3 Magnetic measurements

The magnetic characterization measurements were performed using SQUID magnetometry (Quantum Design MPMS). The critical current densities were calculated from the magnetization loops using the extended Bean model for rectangular samples. For SQUID measurements, small samples ($2 \times 2 \times 1.5 \text{ mm}^3$) were cut from the big pellets.

3. Results and discussion

Firstly, we present our main motivation for the microstructure analysis. Figure 3 (a) shows the critical current density, j_c , as a function of applied field for all the MgB₂ samples at two selected temperatures, $T = 10 \text{ K}$ and 30 K . All samples show an nearly exponential decay of j_c with increasing H . The sample with the highest j_c at self-field is HD1200, followed by sample Sin800 (see also Table 1). The sample Sin950 has a lower j_c at self-field, but at fields above 1 T, j_c is higher than all other samples. The inset presents the irreversibility lines, $H_{\text{irr}}(T)$, for all samples. The irreversibility fields, H_{irr} , are determined from the $j_c(H)$ -data using a criterion of 100 Acm^{-2} . At low temperatures, the samples HD1200 and Sin950 have the highest H_{irr} values. When now performing a pinning force scaling analysis of all the data following the model of Dew-Hughes [24,25], we arrive at the situation shown in Fig. 3 (b). Here, we have selected only data at 10 K and 30 K for clarity; for more data see also Ref. [17]. The peak positions in the scaling are important to judge about the active flux pinning mechanism. Peak positions, h_0 , are found between 0.18 and 0.4, which indicates a strong variation of the origin of flux pinning. The samples Sin775 and Sin800 reveal a non-scaling of the data as the 30 K

data yield much higher peak positions as the low-temperature data. In this case, the flux pinning mechanism clearly changes with temperature. Sample Sin950 shows a much smaller shift with temperature and the peak positions obtained indicate pinning at point pins. The sample HD1200 has the lowest peak position of all samples of $h_0 = 0.18$ at 10 K and 0.24 at 30 K, which speaks for a dominating pinning at grain boundaries. In order to explain these differences observed in Fig. 3, the microstructure analysis was performed.

Now, we turn to the EBSD analysis of the MgB_2 samples. Performing EBSD analysis on the mechanically polished surfaces of the sintered MgB_2 samples lead to several problems due to the high porosity of the samples, as the density achieved is only about 50-55 % of the theoretical value. The average grain size of these samples is about 200–400 nm as observed in Refs. [9,10]. On these samples, we could only record some Kikuchi patterns which could be indexed as MgB_2 phase, but no automated EBSD mapping was possible. Furthermore, the sample Sin950 also showed charging problems due to the higher resistivity [20], which is the reason why we have excluded this sample from the further analysis. All this lead us to perform t-EBSD instead of the standard EBSD in order to achieve a higher spatial resolution with reduced charging effects. In contrast to the sintered MgB_2 samples, the highly dense spark-plasma sintered MgB_2 sample was found to work well with the standard EBSD technique.

For the EBSD analysis, we decided to run single phase scans as the XRD data [8-10] did not show any additional peaks of pure Mg or MgO. The EBSD data are presented as spatially resolved mappings. The size of the selected area is in all cases between 5×5 and $9 \times 9 \mu\text{m}^2$. The image (a) gives an inverse pole figure (IPF) map in [001]-direction using a color code, given in the stereographic triangle. The map (b) is a grain size (GS) map in gray scale (scale ranges from black to white on increasing grain size) together with the EBSD-detected boundaries (rotation angle). The map (c) presents the average grain misorientation. In this map, the edge grains are excluded from the analysis. Finally, (d) gives the inverse pole figure of the respective sample section in (0001)

orientation. Figure 4 gives the data obtained on sample Sin775, Fig 5 the data of sample Sin800, Fig. 6 the ones of sample Sin875 and finally, Fig. 7 the data of sample HD1200.

The comparison of the mappings reveal several interesting points:

(i) The grain sizes decreases between the reaction temperatures of 775 °C and 800 °C, but are increasing again upon increasing the reaction temperature irrespective of the preparation technique applied.

(ii) The orientation of the grains in all sample does not show a specific texture, but the inverse pole figures show some remarkable changes, which will be discussed in the following.

(iii) The average misorientation of the grains is the smallest for the sample Sin775, and increases upon increase of the reaction temperature.

The inverse pole figures reveal an interesting behavior: Sample Sin775 shows a maximum (red area) in the center of the triangle, whereas sample Sin800 shows three maxima at the outer edge. Finally, samples Sin875 and HD1200 have two main maxima in the outer edges of the triangle. This observation demonstrates the effect of the reaction temperature on the grain arrangement.

The EBSD-determined graphs as presented in Fig. 8 give an even better insight to the details of the resulting microstructures of the samples. Figure 8 (a) presents the area fraction as function of the EBSD-determined grain size. Here it is remarkable that the samples Sin775 and Sin875 exhibit a quite similar behavior, whereas the sample Sin800 clearly reveals a large amount of small grains in the nanometer range, and the sample HD1200 shows a more uniform distribution, but also the presence of the largest grains of all samples investigated here. The formation of the small grains at temperatures around 800 °C was investigated in detail in Ref. [10]. Another piece of information is given in Table 1 showing the mean grain size for each sample as determined by the EBSD software. Due to the presence of many small grains in the measured region, the mean grain size of sample HD1200 is comparable to that of sample Sin775, while all other samples follow the basic trend. The increase of the grain size on increasing the reaction temperature was also observed in Refs. [17,26]. To validate the EBSD results, we also investigated the grain sizes on fractured surfaces of the respective samples

as depicted in Fig. 9 (a-c). Here, it is required to image the fractured surfaces with secondary electrons (see e.g., Ref. [27]). The small grain sizes of the samples Sin775 (a) and Sin800 (b) are clearly visible in comparison to sample HD1200 (c). For the statistics, we evaluated about 30 grains of each sample. The data obtained in this way are always slightly larger as the EBSD-determined grain sizes, but confirm the trends of the EBSD data presented above.

In contrast to this behavior, the number fraction of the EBSD-determined misorientation angles [Fig. 8 (b)] for all samples are strikingly similar. The grain average neighbor misorientation [Fig. 8 (c)] is also quite similar for all samples. Finally, Fig. 8 (d) shows the EBSD-determined boundary line length as function of the misorientation. Here, the samples Sin775, Sin875 and HD1200 exhibit an equal behavior, and the sample Sin800 is at a completely different level due to the reduced grain size and hence, the increased boundary length. This is also seen in Table 1 with the total grain boundary length (here all GBs are counting having a misorientation $> 10^\circ$). This length increases at low reaction temperatures, and then decreases strongly on further increasing reaction temperature. This behavior is a direct consequence of the small grains obtained at a reaction temperature of about 800 °C, and then the grains are found to grow again. Therefore, the sample Sin800 can exhibit the strongest flux pinning provided by grain boundaries. This result clearly demonstrates the advantage of sintering MgB₂ samples at a temperature of around 800 °C.

In order to obtain a complete picture of the properties of the MgB₂ samples, it is necessary to regard not only the magnetic properties, but as well the electrical resistance of the samples and the resulting grain connectivity. Furthermore, the formation of secondary phase MgB₄ particles at elevated reaction temperatures contributes additional flux pinning at point defects. Table 1 gives the connectivity (measured as $\Delta\rho = \rho(300\text{ K}) - \rho(41\text{ K})$, see Ref. [20]) for some of the samples investigated here. $\Delta\rho$ firstly decreases on increasing the reaction temperature, and then increases again. This behavior is similar to the change in grain size as seen before. The formation of MgB₄ particles at reaction temperatures above 850 °C provides more flux pinning sites in samples Sin875 and Sin950 (see, e.g., Ref. [10]), but the increasing $\Delta\rho$ reduces the current flow between the grains. In contrast to this, the

sample HD1200 profits from the achieved high density, leading to densely packed grains which also improve the connectivity considerably as manifested by the smallest resistance values. On the other hand, the best connectivity and the presence of MgB_4 particles do not overcome the reduced grain boundary pinning due to the increased grain growth at the high reaction temperature.

Finally, we turn to the EBSD analysis of the samples. Performing EBSD on bulk, sintered MgB_2 samples in the standard configuration (i.e., in reflection mode) turned out to be difficult as the samples exhibit grain sizes in the nanometer range. The achievable resolution (= image quality of the detected Kikuchi patterns) depends strongly on the surface quality, which here cannot be as good as in samples with large grains due to the high number of grain boundaries and pores. For such a situation, the t-EBSD technique working in transmission achieves a much better resolution as recently investigated in Ref. [28] using a comparison of experimental data with simulations. The t-EBSD technique enables the EBSD analysis of nearly all types of MgB_2 samples. The sample Sin950 with its low density is too brittle to survive the preparation of a TEM slice. However, the preparation of TEM slices is a costly process, which poses a problem to a general application. For samples of interest, this is feasible especially in combination with TEM analysis. In principle, other TEM sample preparation methods are also suitable to prepare samples for t-EBSD, however, the required thinning procedure of the final sample may become difficult. The handling of the samples using a nanomanipulator and the possibility to select a given area of interest for the EBSD investigation speaks in favor of the FIB-produced TEM slices.

In case that the MgB_2 samples are much closer to the theoretical density, the standard EBSD technique is found to work well yielding also high image quality values. For the present study, it was important to obtain EBSD images at various sintering temperatures, enabling an important comparison to be made. The conclusions we can draw from this analysis directly influence the optimization of the sintering temperature and the sintering time. Here we may state that an ideal MgB_2 sample for most applications should have a small grain size with an increased grain boundary length

for strong flux pinning, but its density must be much closer to the theoretical value as the current samples.

4. Summary

In summary, we have shown that the transmission EBSD technique works well for sintered MgB_2 samples, whereas for samples close to the theoretical density, the standard EBSD technique gives reasonable results as well. The sintered samples prepared at temperatures ranging between 775 °C and 950 °C show at low reaction temperatures a decrease of the grain size, but at reaction temperatures above 800 °C an increasing average grain size. Additionally, the connectivity between the grains becomes worse. Therefore, the flux pinning of the samples prepared at the lowest temperature is the strongest due to the grains in the 100 nm range yielding the longest grain boundary length, which is clearly seen in the EBSD analysis. The sample Sin950 shows increased flux pinning at MgB_4 particles providing strong pinning at point defects, but suffers from a decreasing connectivity of the grains.

Acknowledgements

The collaboration Uds--GREEN is supported by the EU-INTEREG IVa project "GRMN" (Greater Region Magnetism Network), which is gratefully acknowledged.

References

- [1] Johansen T H 2000 "Flux-pinning-induced stress and magnetostriction in bulk superconductors" *Supercond. Sci. Technol.* **13** R121-R137
- [2] Buzea C and Yamashita T 2001 "Review of the superconducting properties of MgB₂" *Supercond. Sci. Technol.* **14** R115-R146
- [3] Scanlan R M, Malozemoff A P and Larbalestier D C 2004 "Superconducting materials for large scale applications" *Proc. IEEE* **92** 1639-1654
- [4] K. Vinod, Abhilash Kumar R G and Syamaprasad U 2007 "Prospects for MgB₂ superconductors for magnet application", *Supercond. Sci. Technol.* **20** R1-R13
- [5] Tomsic M, Rindfleisch M, Yue J, McFadden K, Phillips J, Sumption M D, Bhatia, M, Bohnenstiel S and Collings E W 2007 "Overview of MgB₂ superconductor applications", *Int. J. Appl. Ceram. Technol.* **4** 250-259
- [6] Putti M and Grasso G 2011 "MgB₂, a two-gap superconductor for practical applications" *MRS Bull.* **36** 608-613
- [7] Larbalestier D C, Cooley L D, Rikel M O, Polyanskii A A, Jiang J, Patnaik S, Cai X Y, Feldmann D M, Gurevich A, Squitieri A A, Naus M T, Eom C B, Hellstrom E E, Cava R J, Regan K A, Rogado N, Hayward M A, He T, Slusky J S, Khalifah P, Inumaru K and Haas M 2001 "Strongly linked current flow in polycrystalline forms of the superconductor MgB₂" *Nature* **410** 186-189
- [8] Muralidhar M, Ishihara A, Suzuki K, Fukumoto Y, Yamamoto Y and Tomita M 2013 "Optimization of the fabrication process for high trapped field MgB₂ bulks", *Physica C* **494** 85-88
- [9] Muralidhar M, Inoue K, Koblishka M R, Tomita M and Murakami M 2014 "Optimization of processing conditions towards high trapped fields in MgB₂ bulks" *J. Alloys Compounds* **608** 102-109
- [10] Muralidhar M, Nozaki K, Kobayashi H, Zeng X L, Koblishka-Veneva A, Koblishka M R, Inoue K and Murakami M 2015 "Optimization of sintering conditions in bulk MgB₂ material for improvement of critical current density" *J. Alloys Compounds* **649** 833-842
- [11] Mikheenko P, Martinez E, Bevan A, Abell J S and MacManus-Driscoll J L 2007 "Grain boundaries and pinning in bulk MgB₂" *Supercond. Sci. Technol.* **20** S264-S270
- [12] Mikheenko P 2012 "Electron backscatter diffraction of MgB₂" *J. Phys. Conf. Ser.* **371** 012064
- [13] Xiao B P, Zhao X, Spradlin J, Reece C E, Kelley M J, Tan T and Xi X X 2012 "Surface impedance measurements of single crystal MgB₂ films for radiofrequency superconductivity applications" *Supercond. Sci. Technol.* **25** 095006

- [14] Trimby P W 2012 "Orientation mapping of nanostructured materials using transmission Kikuchi diffraction in the scanning electron microscope" *Ultramicroscopy* **120** 16-24
- [15] Keller R R and Geis R H 2012 "Features of transmission EBSD and its applications", *J. Microscopy* **245** 245-251
- [16] Yeoh W K, Cui X Y, Gault B, De Silva K S B, Xu X, Liu H W, Yen H W, Wong D, Bao P, Larson D J, Martin I, Li W X, Zheng R K, Wang X L, Dou S X and Ringer S P 2014 "On the roles of graphene oxide doping for enhanced supercurrent in MgB₂ based superconductors" *Nanoscale* **6** 6166
- [17] Wong D C K, Yeoh W K, Trimby P W, De Silva K S B, Bao P, Li W X, Xu X, Dou S X, Ringer S P and Zheng R K 2015 "Characterisation of nano-grains in MgB₂ superconductors by transmission Kikuchi diffraction" *Scripta Mater.* **101** 36-39
- [18] Koblishka M R, Wiederhold A, Muralidhar M, Inoue K, Hauet T, Douine B, Berger K, Murakami M and Hartmann U 2014 "Development of MgB₂-based bulk supermagnets", *IEEE Trans. Magn.* **50** 9000504
- [19] Noudem J G, Aburras M, Bernstein P, Chaud X, Muralidhar M and Murakami M 2014 "Development in processing of MgB₂ cryo-magnet superconductors", *J. Appl. Phys.* **116** 163916
- [20] Wiederhold A, Koblishka M R, Inoue K, Muralidhar M, Murakami M and Hartmann U 2015 "Electric measurements on bulk, polycrystalline MgB₂ samples prepared at various reaction temperatures", presented at PASREG 2015, 2.9.-4.9.2015, Liège, Belgium, to be published in *J. Phys. Conf. Ser.*
- [21] Koblishka M R and Koblishka-Veneva A 2013 "Applications of the electron backscatter diffraction technique to ceramic materials" *Phase Transitions* **86** 651-660
- [22] Koblishka-Veneva A, Koblishka M R, Schmauch J, Chen Y and Harris V G 2010 "EBSD analysis of the microtexture of Ba-hexaferrite samples", *J. Phys. Conf. Ser.* **200** 082014
- [23] Koblishka-Veneva A, Koblishka M R, Mücklich F, Ogasawara K and Murakami M 2005 "Interactions of Y₂BaCuO₅ particles and the YBCO matrix within melt-textured YBCO samples studied by means of electron backscatter diffraction" *Supercond. Sci. Technol.* **18** S158-63
- [24] Dew-Hughes D 1974 "Flux pinning mechanisms in type II superconductors" *Philos. Mag.* **30** 293-305
- [25] Sandu V 2012 "Pinning force scaling and its limitation in intermediate and high-temperature superconductors" *Mod. Phys. Lett. B* **26** 1230007
- [26] Varghese N, Vinod K, Rao A, Kuo Y K and Syamaprasad U 2009 "Enhanced superconducting properties of bulk MgB₂ prepared by in situ powder-in-sealed-tube method" *J. Alloy Compounds* **470** 63-66

- [27] Xu X, Sumption M, Peng X and Collings, E W 2014 "Refinement of Nb₃Sn grain size by the generation of ZrO₂ precipitates in Nb₃Sn wires" *Appl. Phys. Lett.* **104** 082602
- [28] van Bremen R, Ribas Gomes D, de Jeer L T H, Ocelik V and De Hosson J Th M 2016 "On the optimum resolution of transmission-electron backscattered diffraction (t-EBSD)" *Ultramicroscopy* **160** 256-264

Figure captions

Fig. 1. TEM slice prepared from a MgB₂ bulk sample by means of FIB milling. The inset shows some details of the sample Sin775.

Fig. 2. Arrangement of the TEM-slice sample holder in the SEM chamber, inclined by -20 degrees which enables the same detector position to be used as for standard EBSD. The inset shows the custom-built sample holder.

Fig. 3. The critical current densities, $j_c(H)$, and the pinning force, F_p , scaling at $T = 10$ K and 30 K of the MgB₂ samples; other temperatures were omitted for clarity. (a) presents the current densities, and the inset the irreversibility lines of all samples. The blank part of the $j_c(H)$ -curve at 10 K of sample HD1200 is due to flux jumps. (b) gives the pinning force scaling.

Fig. 4. EBSD analysis of sample Sin775. (a) is the inverse pole figure (IPF) map in (001)-direction. The color code for the orientations is given in the stereographic triangle. (b) shows a gray-scale grain size map, with the grain boundary misorientations marked in color. The respective color code is given below the map. Map (c) gives the average grain misorientation. The color code is shown on the right side of the map. Here, the edge grains are excluded from the analysis. Finally, (d) gives the inverse pole figure in [001]-direction for the present sample section.

Fig. 5. EBSD analysis of sample Sin800. (a) is the inverse pole figure (IPF) map in (001)-direction. The color code for the orientations is given in the stereographic triangle at Fig. 4 (a). (b) shows a gray-scale grain size map, with the grain boundary misorientations marked in color. The respective color code is given below the map. Map (c) gives the average grain misorientation. The color code is

shown on the right side of the map. Here, the edge grains are excluded from the analysis. Finally, (d) gives the inverse pole figure in [001]-direction for the present sample section.

Fig. 6. EBSD analysis of sample Sin875. (a) is the inverse pole figure (IPF) map in (001)-direction. The color code for the orientations is given in the stereographic triangle at Fig. 4 (a). (b) shows a gray-scale grain size map, with the grain boundary misorientations marked in color. The respective color code is given below the map. Map (c) gives the average grain misorientation. The color code is shown on the right side of the map. Here, the edge grains are excluded from the analysis. Finally, (d) gives the inverse pole figure in [001]-direction for the present sample section.

Fig. 7. EBSD analysis of sample HD1200. (a) is the inverse pole figure (IPF) map in (001)-direction. The color code for the orientations is given in the stereographic triangle at Fig. 4 (a). (b) shows a gray-scale grain size map, with the grain boundary misorientations marked in color. The respective color code is given below the map. Map (c) gives the average grain misorientation. The color code is shown on the right side of the map. Here, the edge grains are excluded from the analysis. Finally, (d) gives the inverse pole figure in [001]-direction for the present sample section.

Fig. 8. EBSD-determined graphs of all samples under study. (a) shows the area fraction as function of the grain size, (b) gives the distribution of the misorientation angles, (c) shows the average grain neighbor misorientation and (d) the boundary line length per area as function of the misorientation.

Fig. 9. Backscatter electron images of broken surfaces of samples Sin775 (a), Sin800 (b) and HD1200 (c) for comparison with the EBSD data.

Table 1: Data of all samples under study. The $T_{c,onset}$ and the normal-state resistivity [$\rho(41\text{ K})$] are determined by resistance measurements (for details, see Ref. [20]); the critical current density at 20 K and self-field is determined by SQUID measurements.

$\Delta\rho = \rho(300\text{ K}) - \rho(41\text{ K})$ is a measure for the connectivity of the grains, see Ref. [20].

Sample	Sin775	Sin800	Sin875	Sin950	HD1200
$T_{process}$ [°C]	775	800	875	950	1200
Type	sintered	sintered	sintered	sintered	spark-plasma
$T_{c,onset}$ [K]	38.05	38.96	39.95	39.87	38.78
j_c (20 K) [Acm^{-2}]	108.63	135.17	126.32	95.24	321.94
Normal-state resistance $\rho(41\text{ K})$ [$\mu\Omega cm$]	111	57	62	66	5
$\Delta\rho$ [$\mu\Omega cm$]	140	77	107	113	30
EBSD	t-EBSD	t-EBSD	t-EBSD	none	standard
mean grain size [μm]	0.23	0.12	0.33	–	0.24
total GB length per area [μm^{-1}]	12.18	27.66	9.68	–	7.23

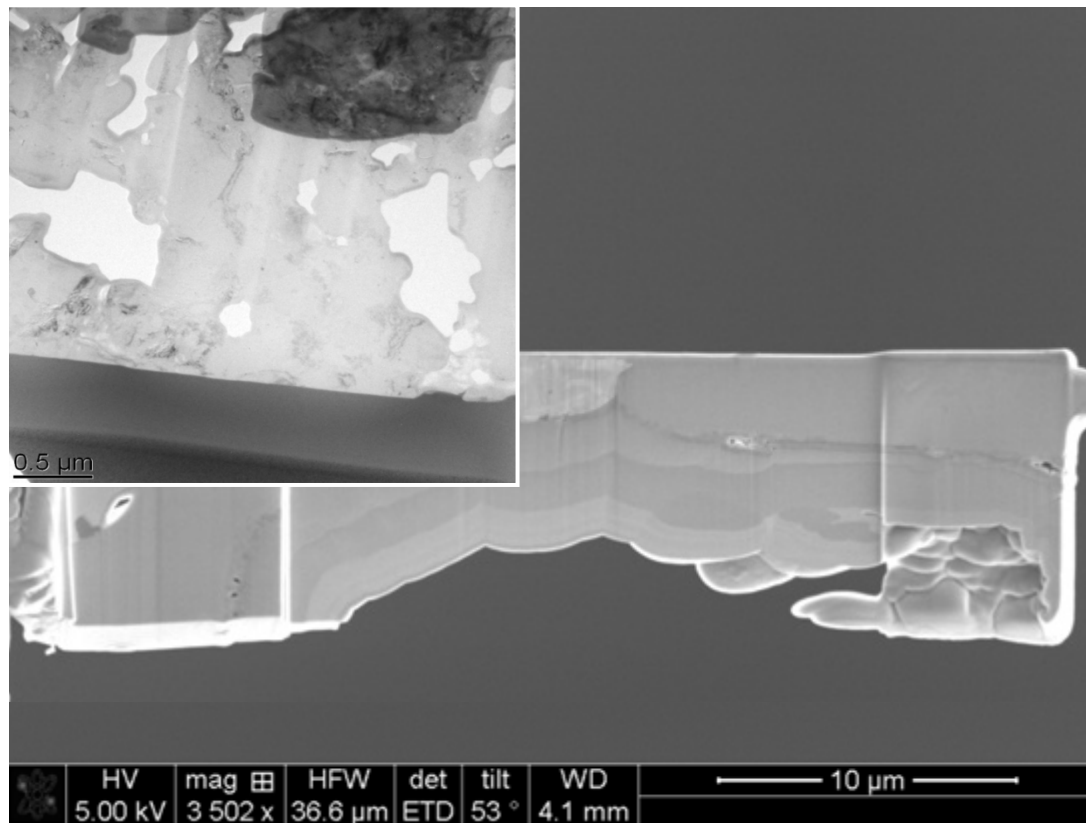


Fig. 1

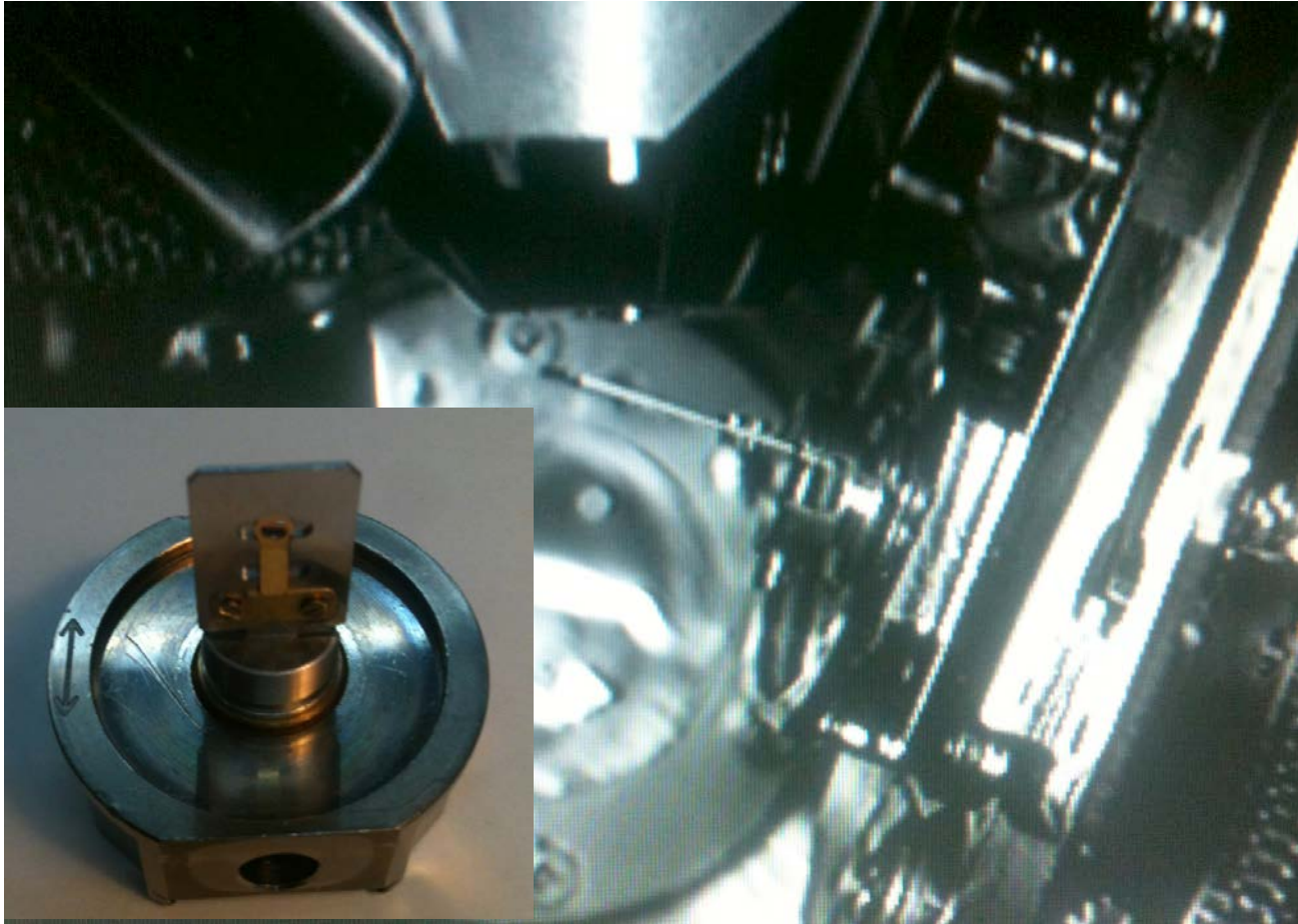


Fig. 2

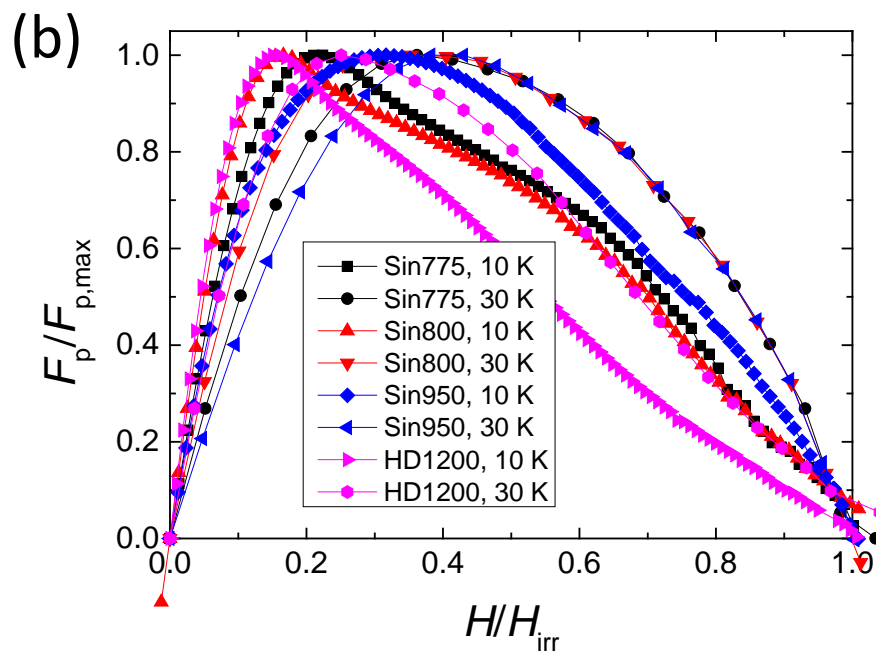
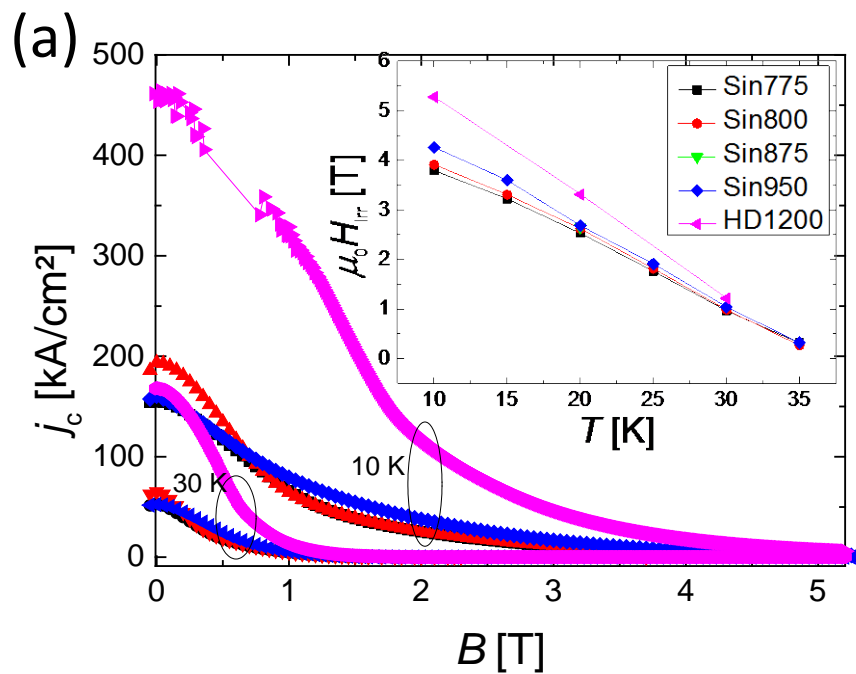
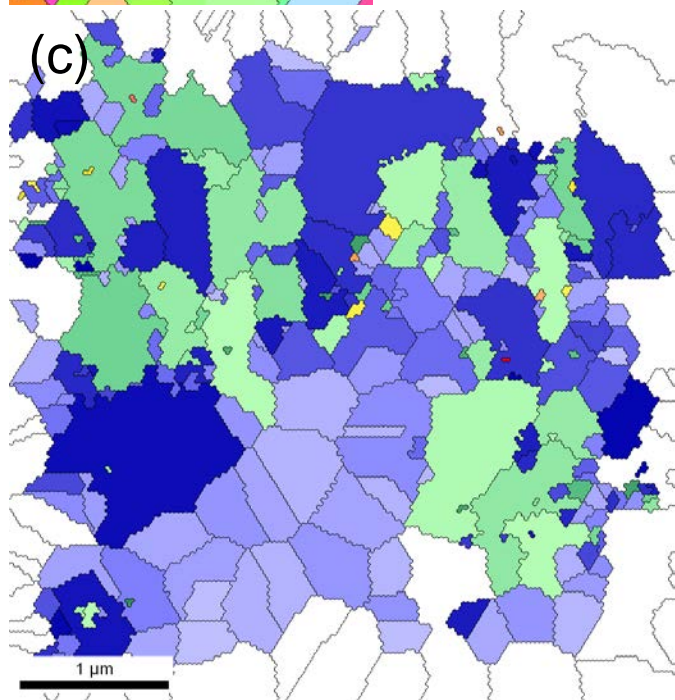
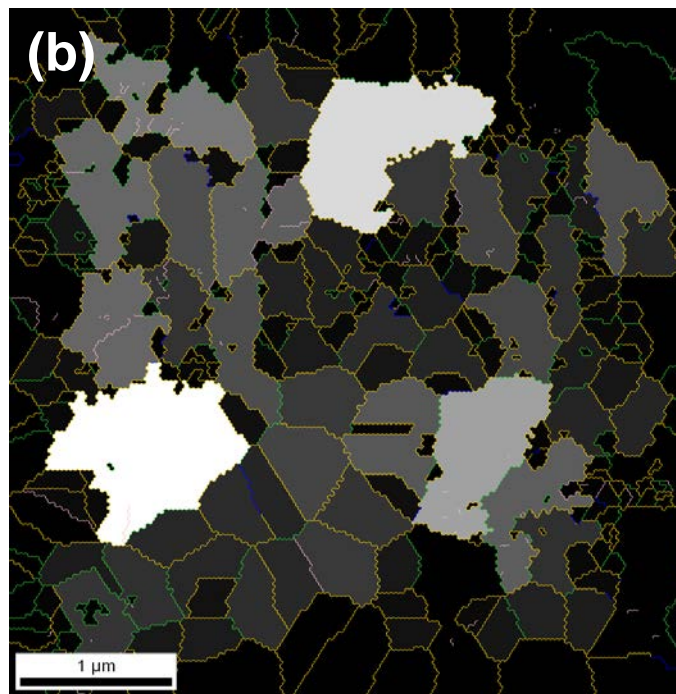
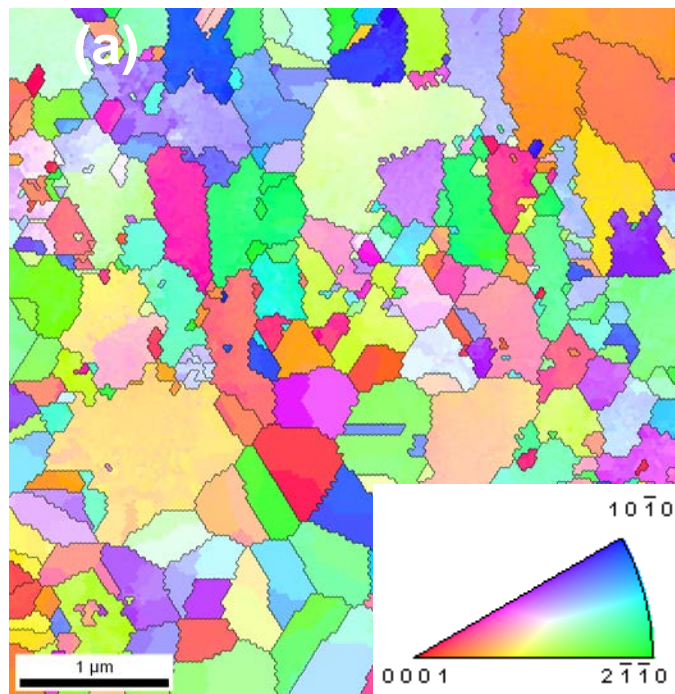











Fig. 3



-  5 – 10°
-  10 – 45°
-  45 – 90°
-  90 – 180°

[001]

-  0 – 0.62
-  0.62 – 1.15
-  1.15 – 1.75
-  1.75 – 1.95
-  1.95 – 2.44

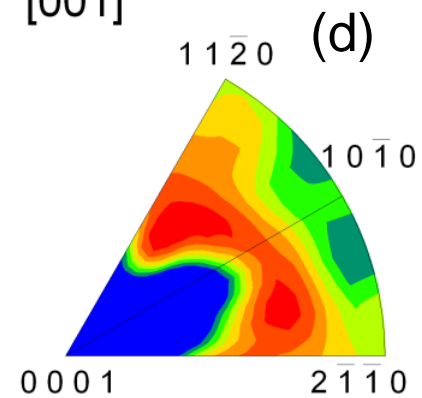


Fig. 4

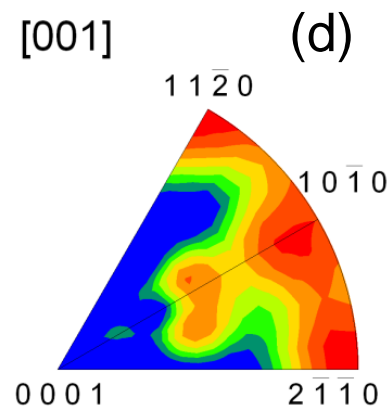
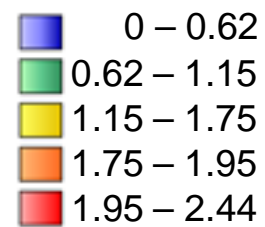
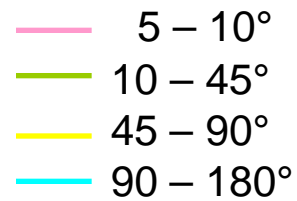
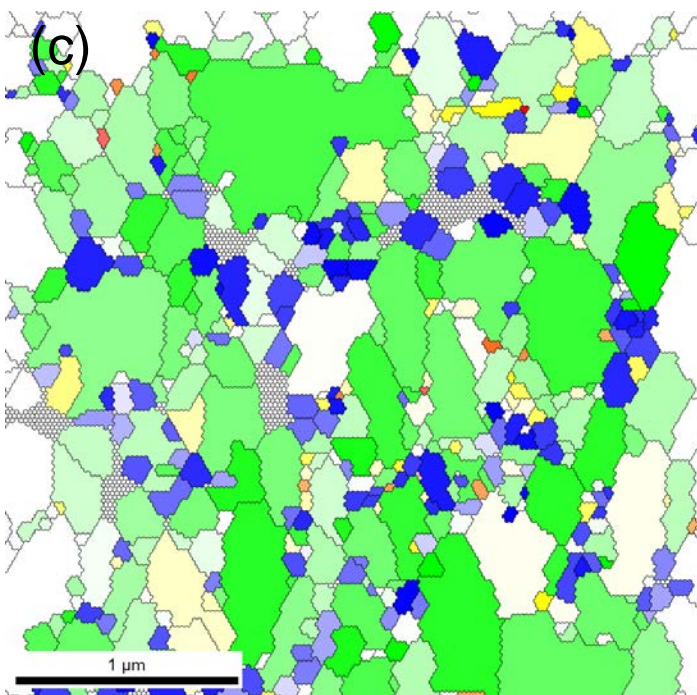
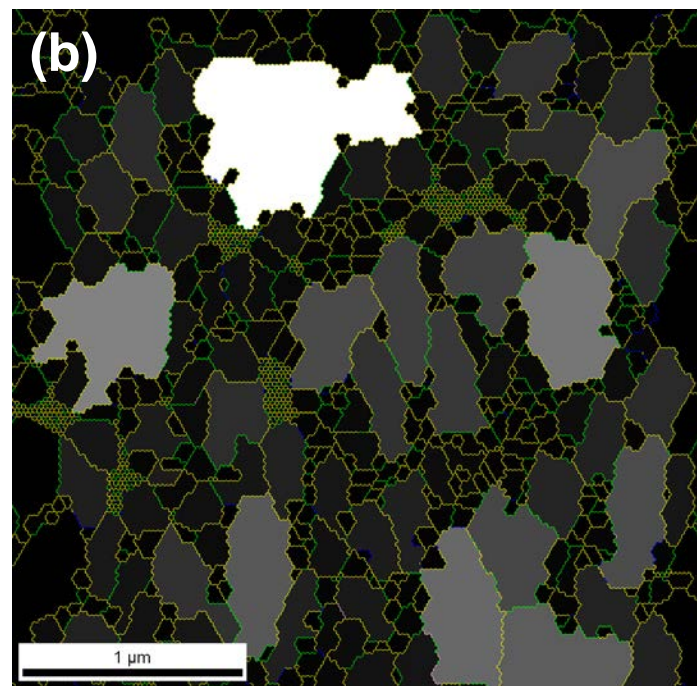
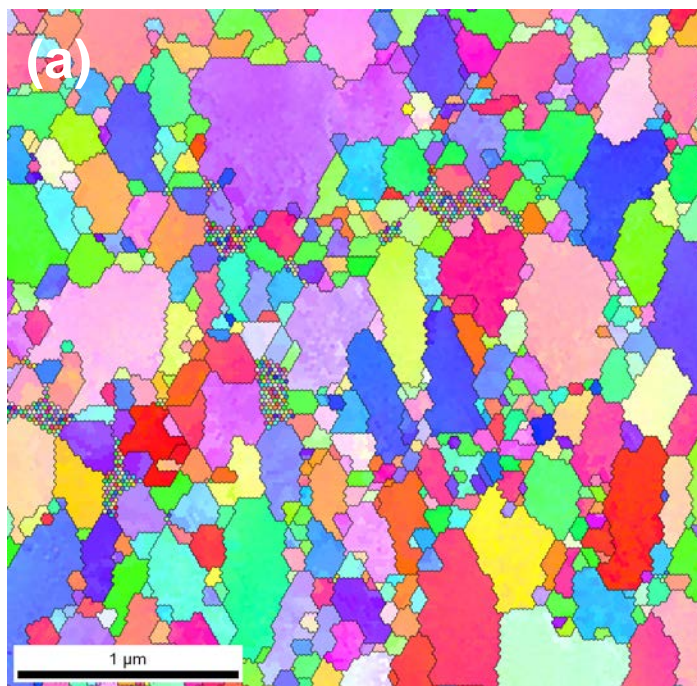
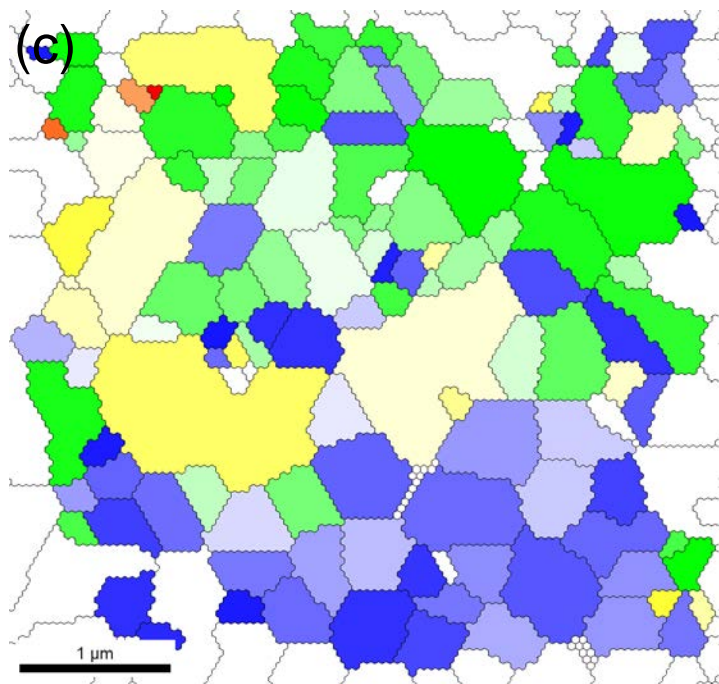
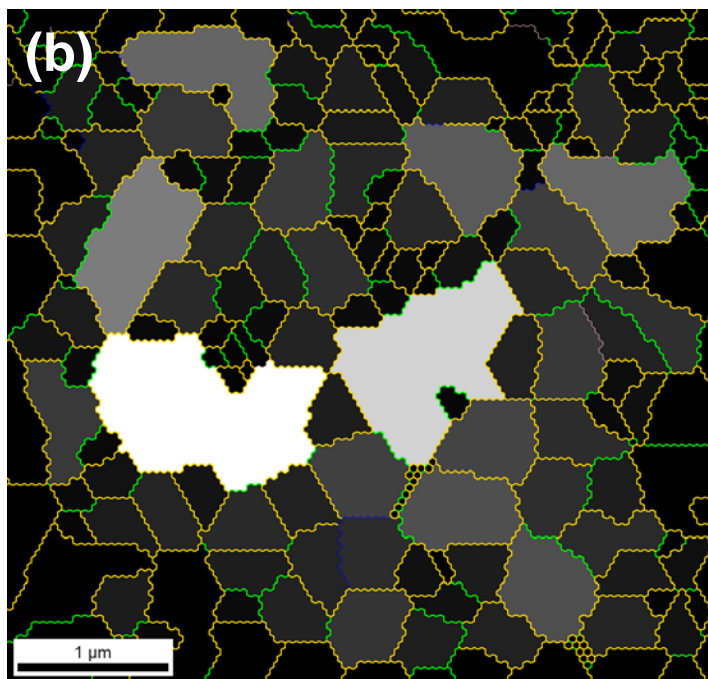
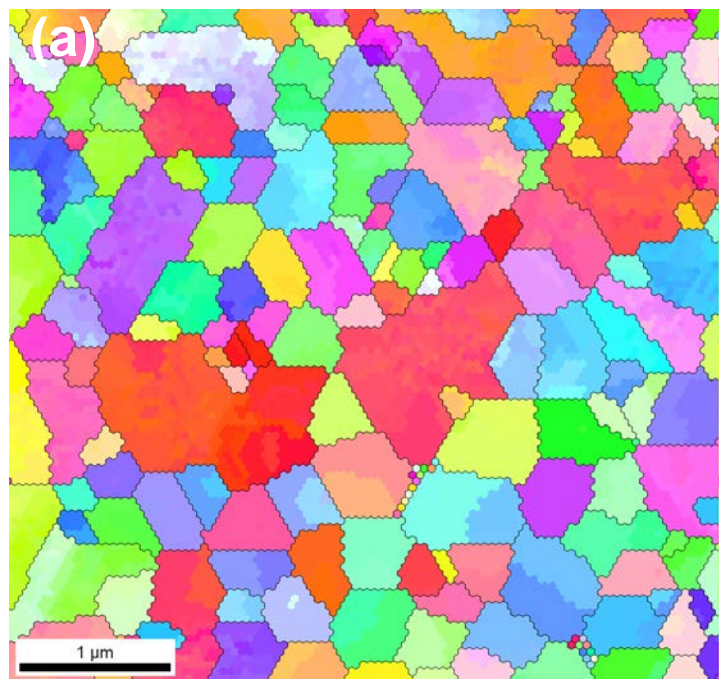


Fig. 5



- 5 – 10°
- 10 – 45°
- 45 – 90°
- 90 – 180°

- 0 – 0.62
- 0.62 – 1.15
- 1.15 – 1.75
- 1.75 – 1.95
- 1.95 – 2.44

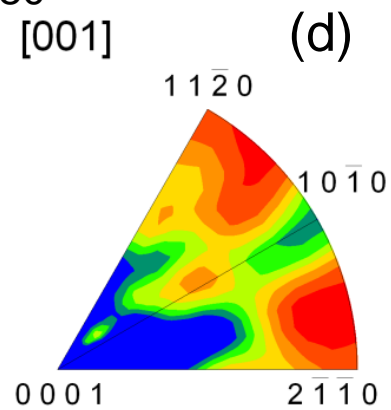


Fig. 6

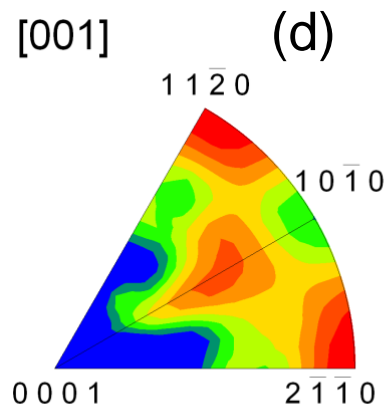
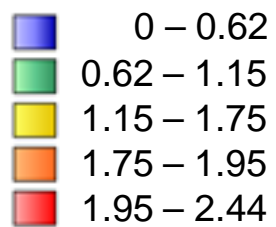
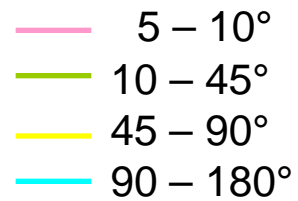
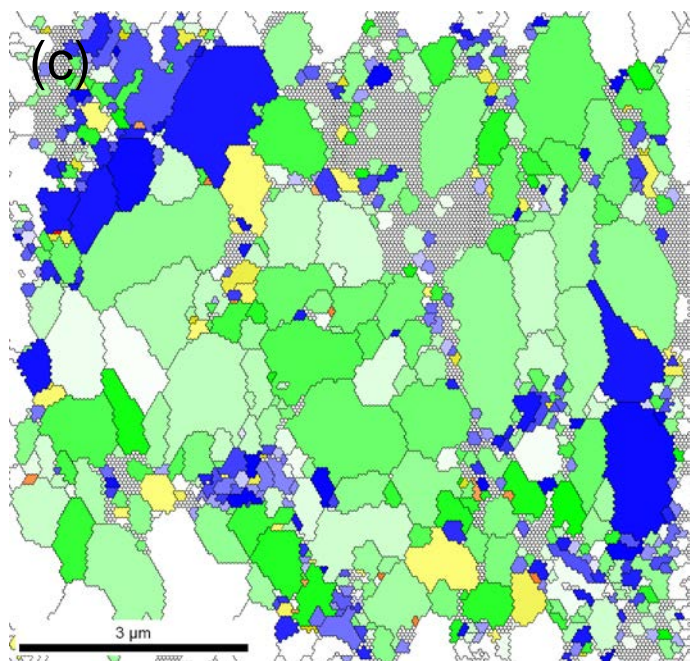
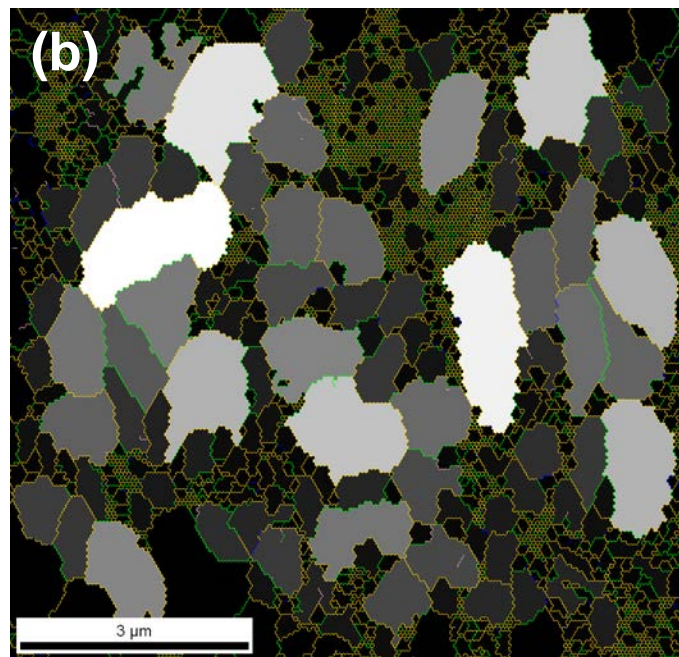
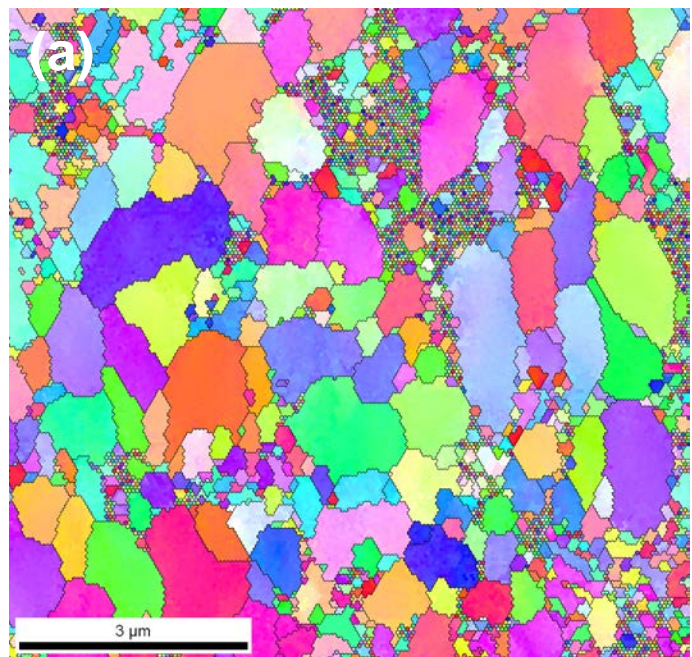


Fig. 7

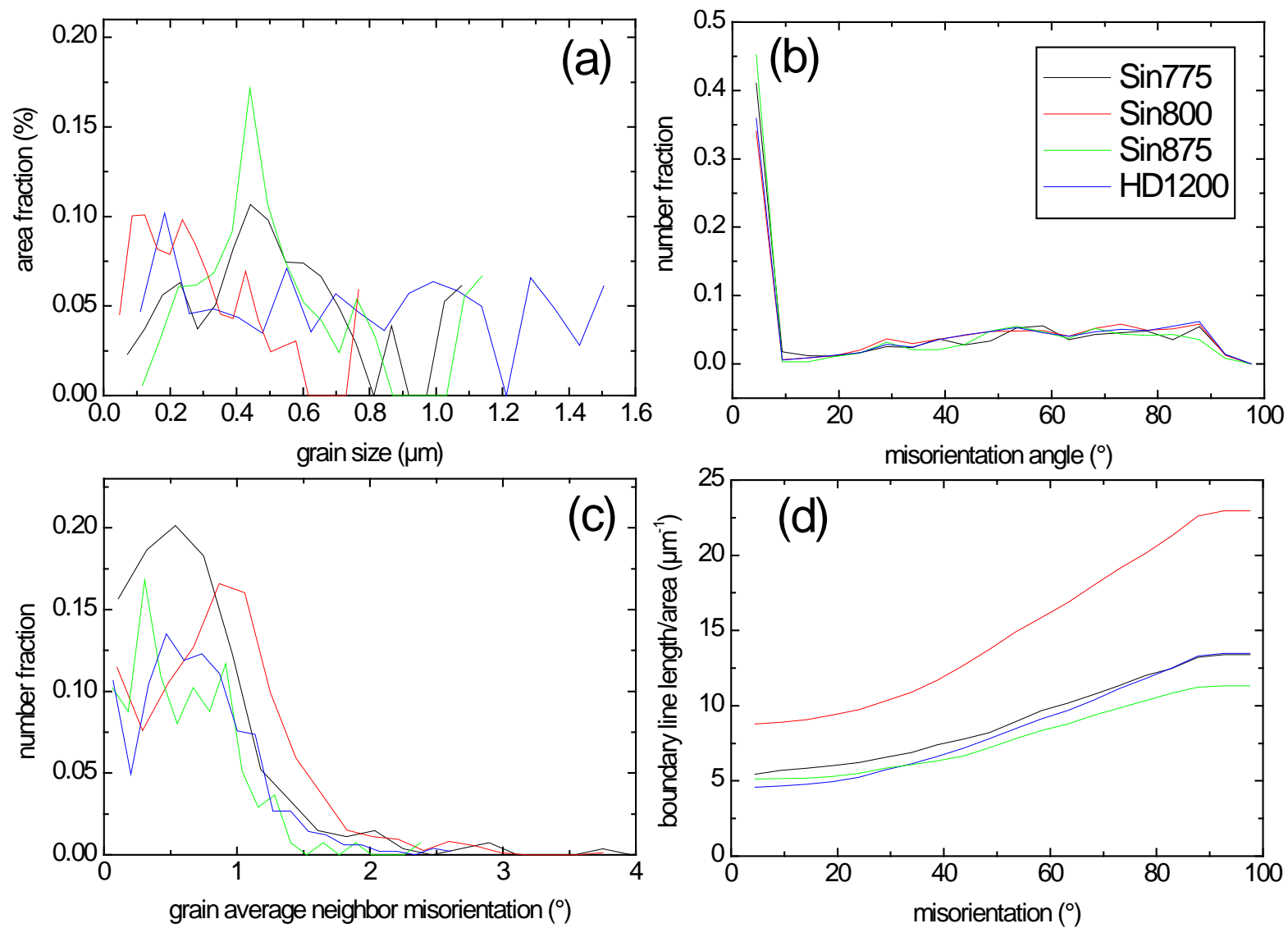
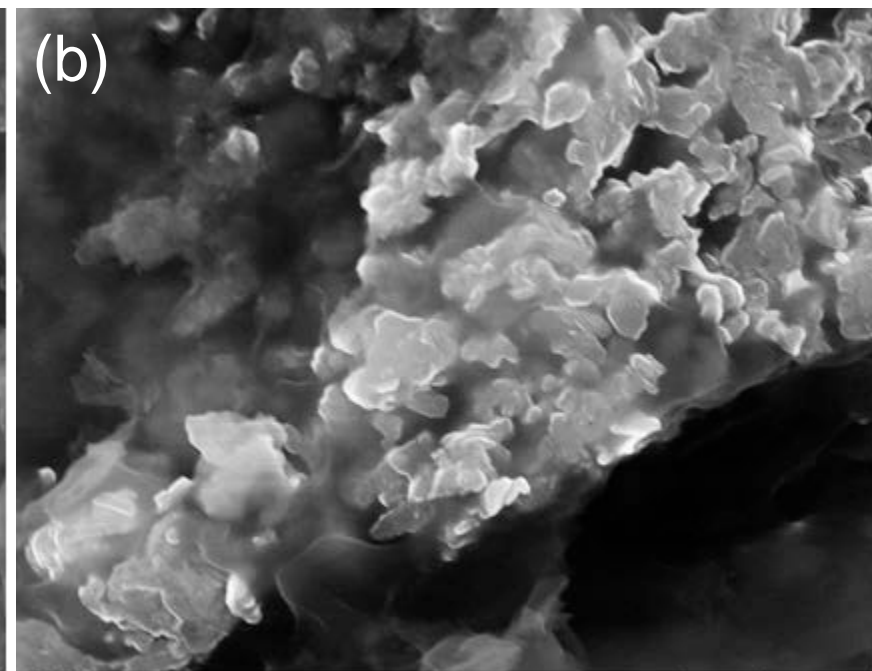
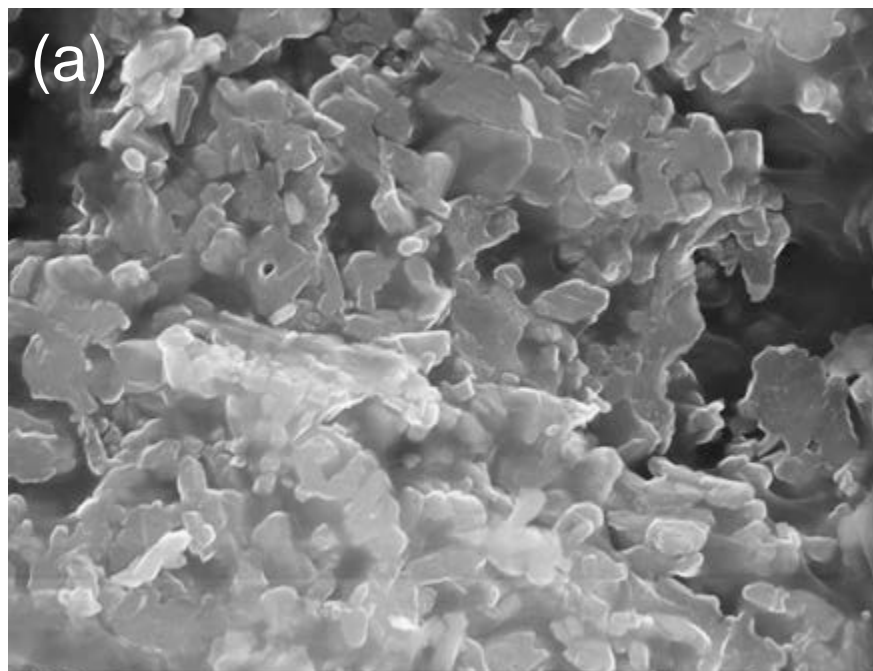


Fig. 8

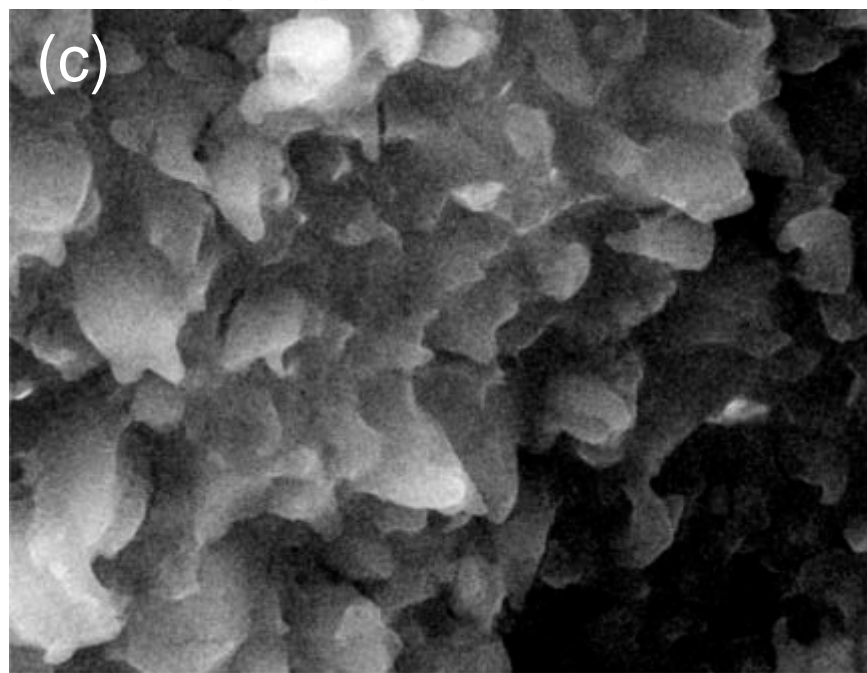


10000x

3 μm

10000x

3 μm



10000x

3 μm

Fig. 9